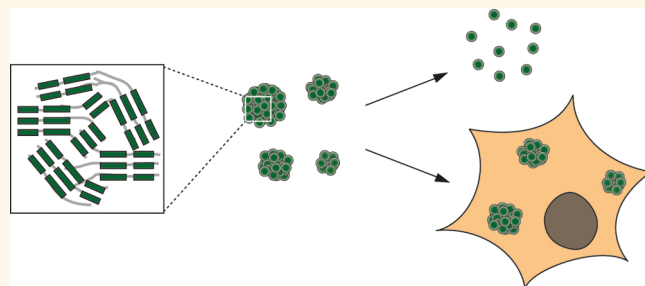


Structure and Biomedical Applications of Amyloid Oligomer Nanoparticles

Senthil T. Kumar,[†] Jessica Meinhardt,[‡] Ann-Kathrin Fuchs,[§] Tobias Aumüller,[†] Jörg Leppert,[‡] Berthold Büchele,[§] Uwe Knüpfer,^{||} Ramadurai Ramachandran,[‡] Jay Kant Yadav,[†] Erik Prell,^{||} Isabel Morgado,[#] Oliver Ohlenschläger,[‡] Uwe Horn,^{||} Thomas Simmet,[§] Matthias Görlach,^{*,‡} and Marcus Fändrich^{*,†}

[†]Institute for Pharmaceutical Biotechnology, Ulm University, 89081 Ulm, Germany, [‡]Leibniz Institute for Age Research, Fritz-Lipmann Institute (FLI), 07745 Jena, Germany, [§]Institute of Pharmacology of Natural Products and Clinical Pharmacology, Ulm University, 89081 Ulm, Germany, ^{||}Leibniz Institute for Natural Product Research and Infection Biology, Hans-Knöll Institute (HKI), 07745 Jena, Germany, [†]Department of Bioorganic Chemistry, Leibniz Institute of Plant Biochemistry, D-06120 Halle, Germany, and [#]Institute for Biochemistry und Biotechnology, Martin Luther University Halle-Wittenberg, D-06120 Halle, Germany. S.T.K. and J.M. contributed equally to this work.

ABSTRACT Amyloid oligomers are nonfibrillar polypeptide aggregates linked to diseases, such as Alzheimer's and Parkinson's. Here we show that these aggregates possess a compact, quasi-crystalline architecture that presents significant nanoscale regularity. The amyloid oligomers are dynamic assemblies and are able to release their individual subunits. The small oligomeric size and spheroid shape confer diffusible characteristics, electrophoretic mobility, and the ability to enter hydrated gel matrices or cells. We finally showed that the amyloid oligomers can be labeled with both fluorescence agents and iron oxide nanoparticles and can target macrophage cells. Oligomer amyloids may provide a new biological nanomaterial for improved targeting, drug release, and medical imaging.



KEYWORDS: peptide assembly · delivery systems · protein misfolding · cell penetration · neurodegeneration

Amyloid oligomers are polypeptide aggregates that are usually β -sheeted and best known from protein misfolding diseases, such as Alzheimer's, Parkinson's, and type II diabetes.^{1–3} They often possess a spheroid particle structure with lateral dimensions of up to 50 nm.^{4,5} The number of molecules contained in these states ranges from two to several hundred polypeptide chains. Administered to neuronal cells or circuits, oligomers can exhibit toxic activities, although there are variations in the biological activity between different oligomeric preparations.^{6,7} Toxic activities have been associated with oligomers that possess hydrophobic surface properties as defined by dye binding,^{8,9} whereas aggregates exposing less hydrophobic surface properties as assessed with this method were found to be less toxic.¹⁰

Oligomers are intermediates of amyloid fibril formation and differ from these more elongated structures by a lower periodicity. Amyloid fibrils are significantly nanostructured

and present a regular 4.7–4.8 Å repeat in the direction of the main fibril axis and a more variable ~10 Å spacing in the direction perpendicular to it.^{11,12} In Alzheimer's disease, amyloid fibrils and oligomers are formed from the amyloid- β (A β) peptide,¹³ and formation of these states can be influenced by the addition of nanoparticles.¹⁴

Besides the pathogenic involvement of amyloid, there is an increasing number of publications that describe amyloid fibrils to also occur as native protein states *in vivo* and carry out important biological functions.^{15–18} These "functional amyloids" prompted concepts to use amyloid fibrils for technical and applicative purposes, for example, as conducting nanowires, cell-support systems, transduction enhancers, hydrogels, or nanostructured biofilms.^{19–22} Such applications are backed up by a wealth of biophysical data that are available on fibrils, describing their global topology, residue-specific structure,^{23–25} physico-elastic properties, and nanoscale material constants like Young's and shear modulus.^{26,27}

* Address correspondence to marcus.faendrich@uni-ulm.de, mago@fli-leibniz.de.

Received for review November 21, 2013 and accepted October 15, 2014.

Published online October 22, 2014
10.1021/nn503960h

© 2014 American Chemical Society

The wealth of data available on fibrils significantly exceeds our insight into the structural utility of amyloid oligomers. This lack of knowledge partly originates from the fact that only a few oligomers could be analyzed in terms of their backbone Ψ/Φ dihedral angles^{28–31} or atomic structures.³² Nevertheless, the small particle size and high surface to mass ratio suggest that they have high specific activities and exhibit an even more advanced applicative potential than fibrils. It is, in fact, consistent with the assumption of a high specific activity that oligomers are widely thought to play a more prominent role for cellular toxicity than fibrils.³³

In this study, we have explored the applicative potential of amyloid oligomers. We used a sample of $\text{A}\beta(1–40)$ peptide oligomers that is specifically well-characterized and stable in solution for more than 1 month.^{30,34} These benign and unique properties enabled us to employ a broad range of different biophysical methods and to systematically screen fundamental structural properties of oligomeric assemblies. Our data establish amyloid oligomers as a novel type of biodevived nanoparticle with potential utilities in numerous fields.

RESULTS

Negative stain transmission electron microscopy (TEM) shows that the investigated amyloid oligomers present a near-spheroid shape with diameters from 15 to 30 nm (Figure 1a and Supporting Information Figure S1a,b). These particles are substantially more isotropic than fibrils (Figure 1b), and more than 70% of the oligomers possess an aspect ratio between 1.0 and 1.5 (Supporting Information Figure S1c). Attenuated total reflectance Fourier transform infrared (ATR-FTIR) spectroscopy demonstrates high levels of β -sheet conformation (Supporting Information Figure S2). Decomposition of the amide I band yields a β -sheet content of more than 50% (Supporting Information Table S1). X-ray diffraction (XRD)-measured Bragg spacings at 4.73 ± 0.03 and 10.15 ± 0.08 Å (Figure 1c) are further compatible with β -sheeted conformations³⁵ and match typical amyloid fibril characteristics, which occur for $\text{A}\beta$ fibrils at 4.73 ± 0.02 and 10.35 ± 0.19 Å (Figure 1d). Interestingly, fibrils have a much more prominent 4.7 Å spacing, indicating much higher periodicity of the structure underlying this spacing, which is stacked up in fibrils along their main axis.

The diffractive properties of oligomers, which are consistent with recent observations,³⁵ demonstrate a significantly nanostructured particle architecture and reveal the presence of nascent elements of amyloid conformation. Combined with a lack of discernible long-range translational symmetries and periodicity, amyloid oligomers qualify as quasi-crystalline assemblies (Figure 1e). Proteolysis of oligomers with proteinase K or subtilisin demonstrates oligomers to be more resistant

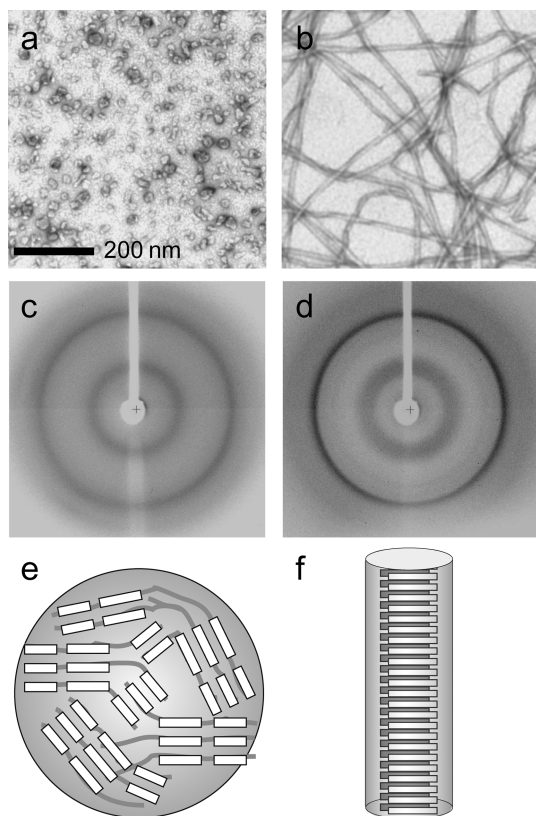


Figure 1. Particle structure and nanostructured order. (a,b) TEM images of oligomers (a) and fibrils (b). (c,d) XRD patterns recorded with randomly oriented oligomers (c) and fibrils (d). (e,f) Schematic representation of the assembly of β -strands of $\text{A}\beta$ peptides in oligomers (e) and fibrils (f).

to proteolysis than the disaggregated peptide (Figure 2a, b) and to exhibit significant structural compactness.

Hydrogen exchange (HX) was used to probe the structural dynamics of oligomers and to identify the oligomeric β -strand conformation underlying their structural compactness. This method depends on the exchange of labile O- or N-bound ^1H hydrogen atoms into deuterium (^2H) (Figure 2c). HX coupled with ATR-FTIR spectroscopy shows a profound loss of the amide II signal (Figure 2d) that occurs within a spectral range from 1500 to 1600 cm^{-1} and that arises from N–H bond vibrations. Peak integral quantifications obtain a greater than 90% reduction of the initial amide II signal after 24 h of exchange, demonstrating almost complete exchange over this period of time. Furthermore, HX was monitored utilizing nuclear magnetic resonance (NMR) spectroscopy. Compact protein conformations, including solvent-occluded core-like elements or stable hydrogen bonds, attenuate exchange (Figure 2c). Therefore, assessment of the backbone amide HX properties with NMR can provide residue-specific information on the presence of stable secondary structural elements. This was demonstrated previously for several amyloid fibrils and related aggregates after their monomerization in deuterated dimethyl sulfoxide ($\text{DMSO}-d_6$).^{36–38}

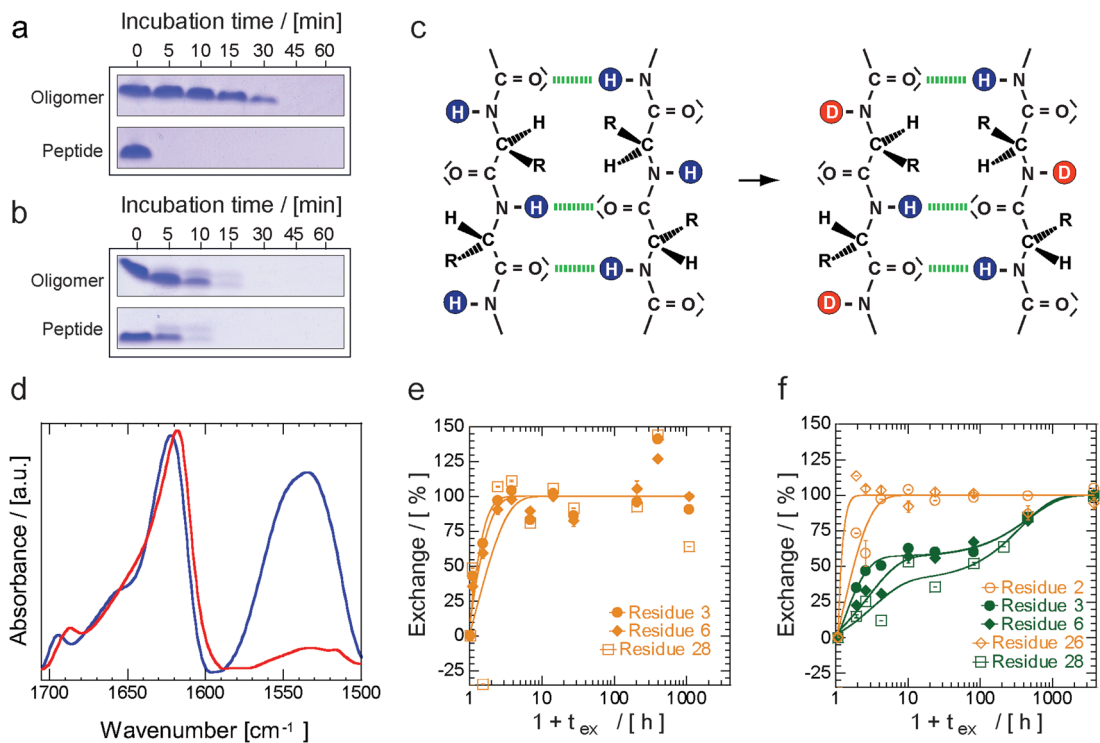


Figure 2. Structural compactness of oligomers and fibrils. (a,b) Digestion of $\text{A}\beta(1-40)$ oligomers and freshly dissolved peptide with proteinase K (a) or subtilisin (b). (c) Schematic representation of the exchange of ^1H (H, blue) into ^2H (D, red). Stable hydrogen bonds also retard exchange, specifically if these occur within secondary structural elements (here a stretch of an antiparallel β -sheet). (d) ATR-FTIR spectra of initially fully protonated oligomers (blue) and after placement in deuterated solvent for 24 h (red). Exchange of amide ^1H hydrogen into ^2H reduces the amide II band ($1500-1600\text{ cm}^{-1}$) to 9% original intensity. (e,f) Progression of HX calculated from plots of the relative NMR peak volumes versus exchange time t_{ex} for individual residues in $\text{A}\beta$ oligomers (e) and fibrils (f). All data in (e) comply with a monophasic fit (ochre). Fibril data (f) display monophasic behavior at residues 2 and 26 (ochre) and a biphasic decay at residues 3, 6, and 28 (green). Error bars indicate standard errors of the extrapolated peak volumes as determined by exponential fitting. End points of the fit were set to 100% exchange.

With regard to our sample of oligomers, we find monophasic exchange characteristics at all analyzed positions of the peptide (Figure 2e). These properties differ significantly from fibril HX, where we see monophasic exchange to be restricted to only certain segments of the peptide, while the remaining positions of $\text{A}\beta$ display biphasic exchange characteristics (Figure 2f). This combination of mono- and biphasic exchange properties is known for $\text{A}\beta$ amyloid fibrils³⁹ and indicates the structural polymorphism of fibrils.^{39–42} Oligomeric exchange rate constants k_{ex} amount to 10^{-1} to 10^1 h^{-1} (Figure 3a), which further contrasts with fibrils that encompass several positions of the peptide in a highly protected state, as shown by exchange rate constants of less than 10^{-1} h^{-1} (Figure 3b). The lowest oligomeric k_{ex} values ($<10^0\text{ h}^{-1}$) occur at residues His6-Glu11, Leu17-Ala21, and Gly25-Gly38 (Figure 3a). Comparison with solid-state NMR data shows that these sites correlate with oligomer β -strand structure (Figure 3c) and importantly include several positions of the peptide N-terminus that form an oligomer-specific β -strand conformation.^{4,30,43}

Next, we sought to investigate the subunit exchange and molecular recycling properties of oligomers. To this end, we used fluorescence spectroscopy and

oligomers prepared from a Glu3Cys variant of $\text{A}\beta$ peptide (Figure 4a) that was site-specifically labeled via maleimide chemistry with different fluorophores such as Alexa Fluor 488 or Alexa Fluor 647. Three types of oligomers were prepared, in which labeled $\text{A}\beta$ was diluted with unlabeled wild-type peptide. Oligomer preparation (i) contained 1% Alexa Fluor 488-labeled $\text{A}\beta$ (AF488- $\text{A}\beta$). Preparation (ii) was prepared from 1% Alexa Fluor 647-labeled peptide (AF647- $\text{A}\beta$), and sample (iii) comprised 1% of a 1:1 mixture of AF488- $\text{A}\beta$ and AF647- $\text{A}\beta$ (Figure 4b–d). The latter sample shows significant Förster resonance energy transfer (FRET), which results in an acceptor band at 671 nm (emission spectrum, Supporting Information Figure S3a) and a donor band at 494 nm (excitation spectrum, Supporting Information Figure S3b). The AF488/AF647 dye pair has a Förster radius of $R_0 \approx 56\text{ \AA}$, and observation of FRET implies a dye to dye distance of less than 80 \AA .

Oligomers containing only AF647- $\text{A}\beta$ lack a donor signal at 494 nm, but addition of preformed AF488- $\text{A}\beta$ oligomers to preformed AF647- $\text{A}\beta$ oligomers produces a marked, time-dependent increase of the donor band at 494 nm (Supporting Information Figure S4a) that implies exchange of monomeric subunits (Figure 4e).

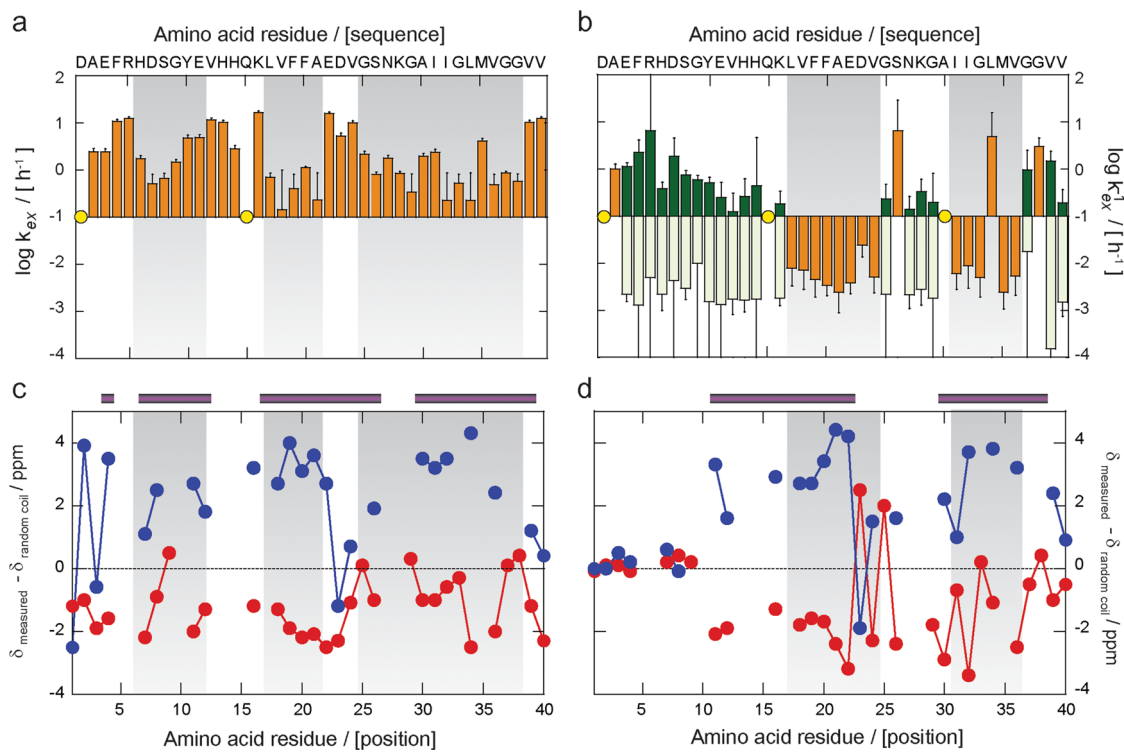


Figure 3. Residue-specific hydrogen exchange and secondary structure. (a,b) NMR spectroscopy-derived residue-specific k_{ex} values plotted against the sequence: (a) oligomers and (b) fibril data. Ochre: data from monophasic fits. Dark green: k_{ex} values from first transitions. Light green: k_{ex} values from second transitions of biphasic fits. Gray shaded areas indicate relatively high protection. Error bars refer to standard error of the exponential fit. Yellow circles mark residues that could not be analyzed. (c, d) Deviation of published ^{13}C - α (red) and ^{13}C - β (blue) chemical shift from random coil values: (c) oligomers and (d) fibril data. Purple bars indicate TALOS-based β -strand assignments as published.^{29,71}

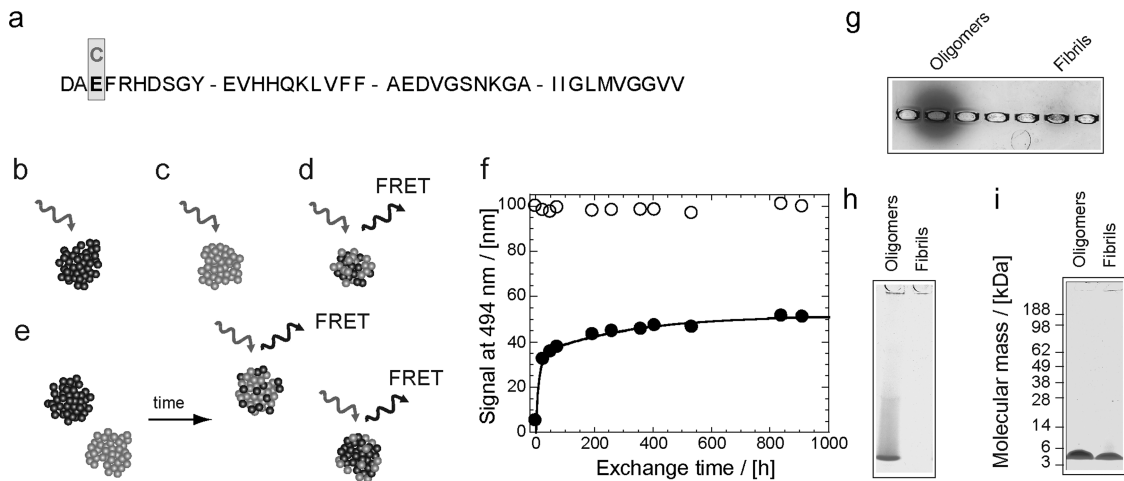


Figure 4. Dynamic assembly and diffusive characteristics of oligomers. (a) Sequence of A β (1–40) peptide and the Glu3Cys variant used for fluorophore labeling. (b–e) Schematic representation of the FRET experiment. AF488-A β (b) or AF647-A β oligomers (c) do not produce any FRET signal (black wave) upon excitation (gray). (d) Oligomers prepared from an equimolar mixture of AF488-A β and AF647-A β show FRET. (e) Subunit exchange enables the time-dependent development of FRET upon mixing preformed AF488-A β and AF647-A β oligomers. (f) Time-dependent FRET obtained by mixing AF488-A β and AF647-A β prior to oligomer formation (empty circle, referenced to 100%) and of a sample, where preformed AF647-A β and AF488-A β oligomers were mixed (filled circle). (g) Diffusion of A β into a 1.5% agarose gel seen with oligomers but not with fibrils. (h) Oligomers applied onto a Coomassie-stained NativePAGE. Fibrils do not enter the gel. (i) Same samples as in (h), run on a Coomassie-stained denaturing PAGE with lithium dodecyl sulfate to disassemble all aggregates into monomers.

Control measurements with sample (iii) show that the FRET efficiency in this sample is stable and does not substantially change within the time frame of the experiment (Figures 4f and S4b). Fitting the

experimental data reveals at least two phases if we mix the two preformed oligomers (Figure 4f). The macroscopic rate constants of these two reactions are $8.8 \times 10^{-2} \pm 2.1 \times 10^{-2}$ and $3.2 \times 10^{-3} \pm 0.8 \times 10^{-3} \text{ h}^{-1}$

and thus smaller than the rate constants of HX of oligomers (Figure 3a). This comparison implies that subunit exchange is slower than hydrogen exchange. Moreover, there is evidence that subunit exchange is incomplete within the time frame of our experiment, as we measure a significantly lower FRET efficiency ($\sim 50\%$) if preformed AF488- $\text{A}\beta$ oligomers were added to preformed AF647- $\text{A}\beta$ oligomers and incubated for several days than in sample (iii), which was prepared by mixing the monomeric peptides AF647- $\text{A}\beta$ and AF488- $\text{A}\beta$ peptides prior to oligomer formation (Figure 4f).

The small spherical architecture of oligomers produces significant diffusible properties, as oligomers possess an increased ability to penetrate into hydrated gel matrices and diffuse more readily into an agarose gel than fibrils (Figure 4g). Oligomeric $\text{A}\beta$ also exhibits higher electrophoretic mobility than fibrils, and oligomers, but not fibrils, enter a native polyacrylamide gel and partially disassemble into monomers (Figure 4h). Denaturing dodecyl sulfate gel electrophoresis, which induces the full disassembly of both oligomers and fibrils, shows consistent migratory characteristics for both samples and confirms the above migratory differences to depend on the assembly state (Figure 4i).

We determined that the oligomeric $\text{A}\beta$ is able to target macrophage cells, which are involved in immunity, tissue repair, and cancer progression. We fluorescently and magnetically labeled oligomers and used flow cytometry to determine cellular interaction. Analysis of the cellular uptake of oligomeric $\text{A}\beta$ revealed that oligomers were preferentially taken up by macrophages as compared to peripheral blood mononuclear cells (PBMCs) (Figure 5a). In fact, within 6 h, up to 98% of the macrophages had taken up fluorescein-labeled $\text{A}\beta$ oligomers, whereas PBMCs showed hardly any increased fluorescence. The fluorescein-tagged $\text{A}\beta$ oligomers were further labeled to generate iron oxide (FeO)- $\text{A}\beta$ nanoparticles by coupling the oligomers with the aid of molecular imprinting technique to polymer-coated superparamagnetic FeO . These FeO - $\text{A}\beta$ particles were also taken up specifically by macrophages (Figure 5b–d), as shown by the increased granularity of macrophages detected by flow cytometric analysis; when cells had been incubated with $\text{A}\beta$ oligomers alone instead of FeO - $\text{A}\beta$ particles, no such increase was observed (Figure 5b). Likewise, we could visualize the internalized particles by confocal microscopy. By three-dimensional (3D) reconstruction, it was assured that the trypsin treatment actually removed all plasma-membrane-bound oligomers or particles (Figure 5c). Finally, differential uptake of FeO - $\text{A}\beta$ particles by macrophages but not by PBMCs was also shown by chemical detection of intracellular iron using the bathophenanthroline method (Figure 5d). Hence, on the basis of their superparamagnetic properties, such multimodal FeO - $\text{A}\beta$ nanoparticles could be used as probes

for macrophages, which might be of special interest for targeted magnetic resonance imaging (MRI) of atherosclerotic lesions.⁴⁴ Likewise, the engineered FeO - $\text{A}\beta$ nanoparticles might assist monitoring the fate of $\text{A}\beta$ by MRI.

DISCUSSION

This research establishes amyloid oligomers as a new class of biocompatible nanoparticles. Structural analysis revealed these states to be compact and to possess a β -sheet assembly (Supporting Information Figures S1 and S2), enhanced resistance to proteolysis (Figure 2a,b), and protection from HX (Figure 3a). HX NMR confirms the position of the oligomeric β -strand structure within the peptide sequence (Figure 3a,c). XRD shows that oligomers are significantly nanostructured and regular, and that they exhibit a lattice-like organization that is able to diffract X-ray beams (Figure 1c). The regularity of the structure of oligomers at the local level contrasts with their lack of long-range periodicity, which thus constitutes one of the major architectural differences to the more elongated and structurally much more periodic assembly of amyloid fibrils. Hence, oligomers are classified by these properties as quasi-crystalline species.

Amyloid oligomers are structurally dynamic and able to undergo an at least partial exchange of their subunits as obtained by FRET analysis (Figure 4f). Native-PAGE further demonstrates their fractional disassembly within an electrical field (Figure 4h). One possible application resulting from these findings is the use of amyloid oligomers as release and delivery systems. Sequestration and release of drugs or nucleic acids has been, in fact, one of the major fields of utility of previously described nanoparticles.⁴⁵ It further relates to applicative utilities of fibrils as deposit forms of pharmacological agents,⁴⁶ functional amyloids that sequester peptide hormones for their subsequent release into the bloodstream,⁴⁷ and the functional fibrils formed from $\text{M}\alpha$ fragment of the Pmel17 protein. These latter filaments enhance the rate of melanin polymerization in the melanosomes of melanocytes because they bind to and organize the biosynthetic melanin precursor 5,6-indolequinone.¹⁶ Amyloid oligomers may thus be used to sequester and release the peptides from which they are constructed and may also be used for nonproteinaceous molecules that are attached to these peptides.

Amyloid oligomers with diameters of typically 15–30 nm (Figure 1 and Figure S1) are considerably smaller than most previously studied nanoparticles which range from 0.1 to 1.0 μm .⁴⁸ Their small size implies highly diffusive characteristics, which is consistent with observations that amyloid oligomers are readily able to enter into gel matrices or living cells (Figures 4g–i and 5a–d) and suggests, taken together with their higher surface to mass ratio, access to more

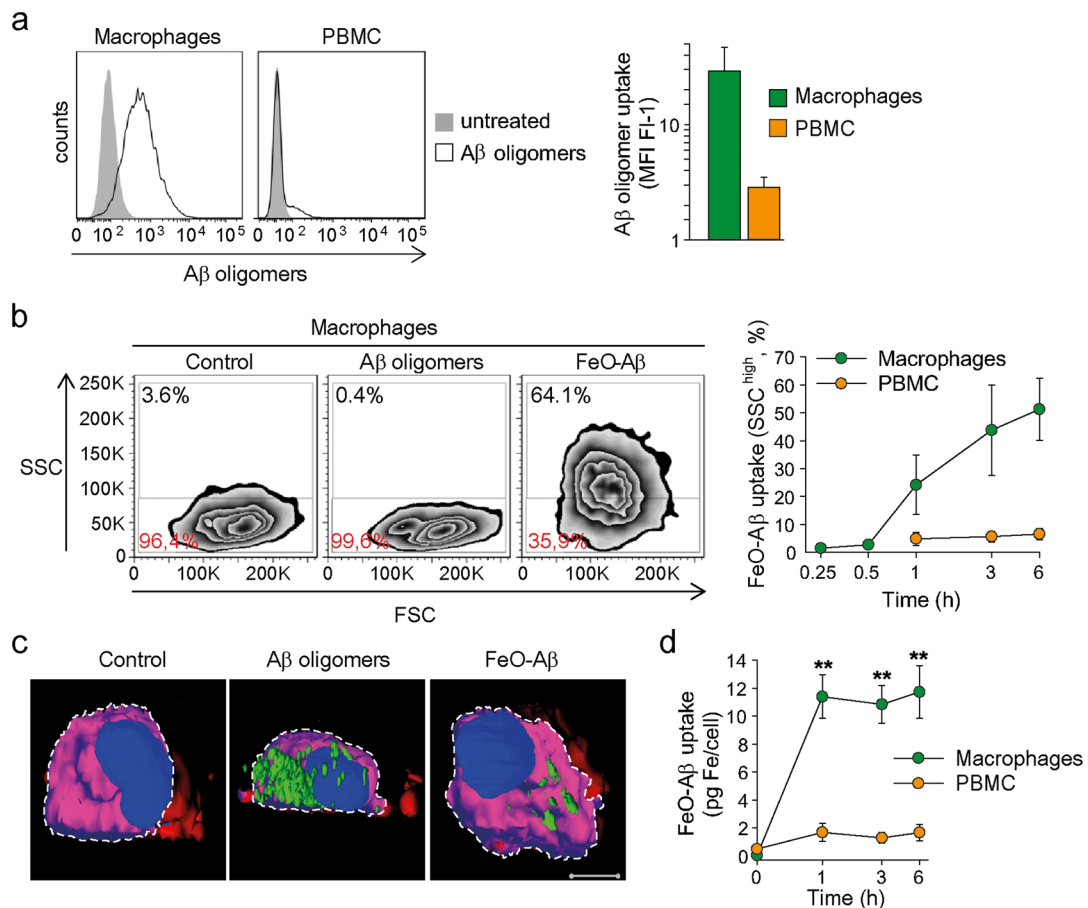


Figure 5. Cell-specific uptake of $\text{A}\beta$ oligomers enables the internalization of iron particles. (a) Human macrophages and PBMC were incubated with $1.15 \mu\text{M}$ fluorescence-labeled $\text{A}\beta$ oligomers for 6 h (h). Cell-membrane-bound $\text{A}\beta$ oligomers were removed by trypsinization, and uptake into cells was analyzed by flow cytometry in channel Fl-1 (ex 488 nm/filter 530/30). Representative histograms are shown. MFI, median fluorescence index, $n = 3$. **(b)** Human macrophages or PBMC were incubated with $1.15 \mu\text{M}$ fluorescein-labeled $\text{A}\beta$ oligomers or $30 \mu\text{g}$ Fe/mL $\text{FeO-A}\beta$ particles. Cells were treated with trypsin to remove cell-membrane-bound particles and analyzed by flow cytometry. Uptake of $\text{FeO-A}\beta$ particles by macrophages is shown as an increase in granularity (FSC: forward scatter). Blots show representative samples after 6 h of treatment. Uptake kinetics of $\text{FeO-A}\beta$ is shown on the right as percentage of cells with an increased side scatter (SSC) signal, $n = 4$. **(c)** Alternatively, cells treated as in (b) were analyzed by confocal microscopy, and 3D surface projections of single macrophages were prepared from Z-stacks. Rendering of the plasma membrane shown in red (view from outside) or pink (view from inside the cell) of the nucleus in blue. The front part of the cell was cut away in the image (cutting edge at the membrane shown as dotted white line). Green $\text{A}\beta$ oligomers/ $\text{FeO-A}\beta$ particles are intracellular. Scale bar: $5 \mu\text{m}$. Data are representative of three independent experiments. The plasma membrane (red) is only partially shown to uncover intracellular structures. **(d)** $\text{FeO-A}\beta$ uptake by macrophages, but not by PBMC, was confirmed by direct measurement of the iron contents. Cells were treated as in (b), $n = 4$, $**p \leq 0.01$. All error bars represent standard error of the mean.

remote sites within a tissue and higher biological activities than fibrils.

Many traditional nanoparticles were formed from nonproteinaceous compounds, including inorganic materials or synthetic organic polymers, such as poly-lactide–polyglycolide copolymers and polyacrylates,⁴⁹ but also albumin, collagen, and chitosan have been used.^{48,49} It is thus another advantage of amyloid oligomers that these are biocompatible and can be readily degraded by natural enzymes, as we show here with proteinase K and subtilisin (Figure 2a,b). This conclusion is not compromised by the potential involvement of oligomeric species in certain protein misfolding diseases, as these effects arise from only particular types of oligomers and as it was shown that also nontoxic oligomers can be prepared from pathogenic polypeptide chains.^{8,9,50}

Amyloid nanoparticles are easy to prepare *in vitro* and can be made available in significant quantities. They are easy to modify and to functionalize, and modifications can be introduced during peptide synthesis, for example, by solid-phase chemical synthesis, molecular genetics, and recombinant protein expression, or they may be added through postsynthesis strategies, such as site-specific chemical coupling. Our present data illustrate these possibilities by introduction of a single Cys residue (Figure 4a) and the subsequent modification of this residue with a fluorophore.

Oligomeric $\text{A}\beta$ is preferentially taken up by macrophages *versus* other peripheral blood mononuclear cells. The small fraction of PBMC that has also taken up labeled $\text{A}\beta$ oligomers most probably represents the monocytes in the population. Therefore, our data

suggest that macrophages can be specifically targeted by $\text{A}\beta$ oligomers. Over recent years, it became more and more evident that macrophages not only are involved in immunity and tissue repair but often play a causative role in disease progression.⁵¹ Apart from well-known pathophysiological processes associated with macrophage activation such as atherosclerosis,^{44,52} fibrosis and even tumor initiation and progression⁵¹ have been linked to macrophage activity. On the basis of our findings, we propose a new possible application of $\text{A}\beta$ oligomers, namely, macrophage targeting. By labeling of superparamagnetic iron oxide particles with oligomeric $\text{A}\beta$, these particles could be specifically targeted to macrophages. In the end, this could be used for the visualization of

disease-associated accumulation of macrophages *in vivo* by MRI.^{53,54} Of particular interest might be the imaging of atherosclerotic plaques to assess the extent of cardiovascular diseases.^{55,56}

CONCLUSIONS

Amyloid oligomers qualify as a novel class of proteinaceous and biocompatible nanoparticles. Future challenges ahead will be to delineate ways to better control the structural homogeneity of these states and to increase their long-term stability in fully aqueous solvents. However, our current data already imply a plethora of potential applications of these or structurally analogous assemblies and their relevance for a range of different disciplines from biological engineering to nanotechnology.

MATERIALS AND METHODS

Preparation of $\text{A}\beta$ Oligomers and Fibrils. Recombinant $\text{A}\beta(1-40)$ peptide, including fully ^{15}N -labeled $\text{A}\beta(1-40)$ peptide, was produced in-house by using a recombinant expression system for *Escherichia coli*.^{57,58} The methods of fibril formation⁴⁰ and oligomer formation³⁰ have been detailed elsewhere.

Hydrogen Exchange. Isotope-enriched chemicals were purchased from Eurisotop. $^1\text{H}/^2\text{H}$ exchange of oligomers was initiated by freezing the oligomer sample in liquid N_2 , followed by lyophilization and resuspension in the initial volume of 10% HFIP- $d_2/\text{D}_2\text{O}$. Transmission electron microscopy confirms that lyophilization does not affect the oligomer morphology. Oligomer exchange reactions were performed under quiescent conditions at 0.25 mg/mL concentration, 20 °C and pD^* 3.8 (pH meter reading without correction for isotope effects). At different time points between 0 min and 44 days, an aliquot of the exchanging oligomer sample was taken, and the exchange was stopped by lyophilization. Previous studies established that oligomers are stable under the conditions of exchange for significant time periods (>40 days) and do not further convert into mature fibrils.³⁰

Mature ^{15}N -labeled $\text{A}\beta(1-40)$ fibrils were sedimented by centrifugation at 9400g for 10 min. The supernatant was removed, and the fibril pellet was washed once with 50 mM deuterated sodium borate buffer (pD^* 7.8). Afterward, the pellet was resuspended in deuterated borate buffer by pipetting up and down and vigorous vortexing. The HX reaction was performed under quiescent conditions at a concentration of 1 mg/mL and at 20 °C. At different time points between 0 min and 5 months, an aliquot of the exchanging fibril sample was taken and centrifuged at 16 000g for 10 min, followed by washing with D_2O . The fibril pellets were immediately frozen in liquid N_2 to quench HX and kept at 80 °C until measurement.

Nuclear Magnetic Resonance Spectroscopy. NMR experiments were carried out at 25 °C on a Bruker AVANCE III narrow-bore spectrometer operating at 600 MHz (proton frequency) and equipped with a 5 mm triple resonance, pulsed field z-gradient cryoprobe. To monitor $^1\text{H}/^2\text{H}$ exchange with solution-state NMR spectroscopy, oligomers or fibrils had to be disaggregated. Disaggregation was achieved by dissolving the lyophilized oligomers or the wet fibril pellet in perdeuterated dimethyl sulfoxide (DMSO- d_6) containing 0.1% deuterated trifluoroacetic acid (TFA- d_1). Complete dissolution was achieved by vigorous vortexing. NMR experiments were carried out using final $\text{A}\beta$ concentrations of 150–550 μM . The dissolved aggregates were immediately transferred into a Shigemi NMR tube, and within the next 3 h, a series of 60 two-dimensional band-selective optimized flip-angle short-transient heteronuclear multiple quantum coherence (SOFAST-HMQC) experiments were recorded.⁵⁹

Transmission electron microscopy showed that treatment with DMSO/TFA effectively dissolved all $\text{A}\beta(1-40)$ oligomers

and fibrils before acquisition of the first NMR experiment (≤ 8 min). Thus, well-dispersed $[^1\text{H}, ^{15}\text{N}]$ -correlation spectra were obtained. Only the $[^1\text{H}, ^{15}\text{N}]$ -amide cross-peaks of residues D1, Q15, and L34 in fibrils and of D1 and Q15 in oligomers could not be detected in the HMQC spectra. The chemical shifts of all other backbone amides could be assigned unambiguously by using $^{15}\text{N}, ^{13}\text{C}$ -labeled $\text{A}\beta(1-40)$ peptide and ^{15}N -edited NOESY, ^{15}N -edited TOCSY, $[^1\text{H}, ^{13}\text{C}]$ -HSQC, ^{13}C -edited NOESY, HNCACB, HNCO, HNCACO, CCCONH, and HCCH-TOCSY triple-resonance experiments. The NMR spectra were processed and analyzed with the program XEASY.⁶⁰

Analysis of the Hydrogen Exchange NMR Data. The program NMRPipe⁶¹ was used to quantify the peak volumes of the $[^1\text{H}, ^{15}\text{N}]$ -amide cross-peaks in each SOFAST-HMQC spectrum. During the workup of the DMSO-dissolved NMR samples (~ 8 min), further forward exchange (^1H to ^2H) in previously protected regions and back exchange (^2H to ^1H) can occur. These processes impede direct recording of the exchange pattern arising from the actual forward exchange (^1H to ^2H) experiment. To compensate for any exchange occurring within the dead time between dissolution of the samples and NMR detection, a series of 60 spectra were recorded within 3 h after NMR sample preparation (see above), and the signal decay of each peak was fitted to a single-exponential function. Based on this fit, the peak volume at the time point of dissolution was extrapolated. The plots of the extrapolated peak volumes *versus* the exchange time t_{ex} revealed monophasic exchange behavior for most residues. For these residues, the decay of the ^1H signal (P_{res}) was fitted to a single-exponential equation, yielding the exchange rate k_{ex} :

$$P_{\text{res}} = A + B e^{-k_{\text{ex}} t_{\text{ex}}}$$

where A and B are fitting constants. Only for some residues and only in the fibril sample, a different exchange pattern was encountered that presented biphasic behavior:

$$P_{\text{res}} = A + B e^{-k_{\text{ex1}} t_{\text{ex}}} + C e^{-k_{\text{ex2}} t_{\text{ex}}}$$

where A , B , and C are fitting constants. Such a biphasic behavior was observed previously for an $\text{A}\beta(1-42)$ fibril sample, probably resulting from structural heterogeneity in these residues.³⁹ The exchange data from these residues were fitted to the sum of two single-exponential equations, thus yielding two k values for one residue. The sum of two exponential functions produced a significantly better fit for these residues as compared with a single-exponential fit, as determined with F-test ($p < 0.05$).

Attenuated Total Reflectance Fourier Transform Infrared Spectroscopy. Immediately prior to ATR-FTIR measurements, residual hexafluoro-2-propanol (HFIP) was removed from the sample of $\text{A}\beta(1-40)$ oligomers by evaporation under a gentle stream of N_2 for 1.5 h. The oligomers were concentrated to 5 mg/mL using

Amicon Ultra-4 centrifugation units with 30 kDa cutoff (Millipore). $\text{A}\beta(1-40)$ fibrils were grown as described above but at a concentration of 5 mg/mL. Infrared spectra were measured in water (oligomers) or in 50 mM sodium borate buffer, pH 7.8 (fibrils). All spectra were acquired on a Bruker Tensor-27 FTIR instrument equipped with a BIO-ATR-II cell and a photovoltaic LN-MCT detector cooled with liquid N_2 . A total of 40 scans were collected at room temperature with an aperture of 4 mm. Three-term Blackman–Harris apodization was applied prior to Fourier transformation. An instrument resolution of 4 cm^{-1} was used with four times zero filling, resulting in a data point resolution of 1 cm^{-1} . Absorbance spectra were corrected for residual solvent absorption by scaled subtraction of the solvent spectrum. To determine the secondary structure fractions, the spectra were processed and decomposed as described.⁶²

X-ray Diffraction. Fibrils were sedimented by ultracentrifugation at 100 000 rpm for 30 min at $4\text{ }^\circ\text{C}$ with a S100AT3-204-100 KRPM rotor in a SORVALL RC-M120GX centrifuge. A portion of the wet pellet was scraped out and placed on the top of Nylon cryoloop (0.3 mm diameter, Hampton Research) for X-ray diffraction. The oligomer solution was centrifuged at 14 000 rpm for 15 min to remove large aggregates. The supernatant, which contains oligomers, was collected and freeze-dried ($-80\text{ }^\circ\text{C}$). Oligomers were placed as lyophilized powder onto the cryoloop and soaked with a droplet of water immediately before submission to X-ray diffraction. X-ray diffraction images were collected at room temperature in an in-house source using an R-AXIS IV++ detector. The distance between sample and detector was set to be 20 cm, and exposure time was adjusted to 60 s. Images were analyzed with the program Crystal Clear 1.3.6SP2, and the diffraction spacings were taken at several points along the reflection arc and averaged.

Transmission Electron Microscopy. Morphological analysis of $\text{A}\beta(1-40)$ oligomer particles was carried out by negative stain transmission electron microscopy. Oligomer particle grids were prepared according to the floating carbon method.⁶³ Specimens were then examined with a Zeiss 900 electron microscope with an acceleration voltage of 80 kV, and images were captured using a built-in CCD camera. For quantitative analysis, oligomer particles were examined in an area of the TEM image, measuring their particle diameters d_1 and d_2 with an ITEM program. Particle diameter d_2 was defined as the larger value. From the particle measurements, aspect ratio (d_2 divided by d_1) was determined. Reported data represent the averages from four independent measurements.

Proteolytic Digests. $\text{A}\beta(1-40)$ oligomers (0.5 mg/mL) and freshly dissolved peptide were incubated with 1 $\mu\text{g}/\text{mL}$ proteinase K (Invitrogen) and subtilisin (Sigma) in 50 mM Tris-HCl buffer, pH 8.2, at $37\text{ }^\circ\text{C}$. Aliquots of 25 μL were removed after incubation for 0, 5, 10, 15, 30, 45, and 60 min, and the reaction was stopped by the addition of phenylmethylsulfonyl fluoride to a final concentration of 5 mM and immediately applied to gel electrophoresis.

Polyacrylamide Gel Electrophoresis. For analysis of the electrophoretic mobility of oligomers and fibrils with NativePAGE, 10 μL of the NativePAGE sample buffer (4 \times) was added to a 30 μL sample solution containing 150 μM $\text{A}\beta$ as oligomers or fibrils. Twenty microliters of these mixtures was loaded on a Native PAGE 4–16% Bis-Tris gel (Invitrogen). These gels were run with NativePAGE 20 \times running buffer (Invitrogen). For analysis of the electrophoretic mobility of oligomers and fibrils with lithium dodecyl sulfate (LDS) PAGE, samples were boiled for 5 min at $95\text{ }^\circ\text{C}$ in NuPAGE LDS sample buffer (4 \times) (Invitrogen) and resolved on 4–12% NuPAGE Bis-Tris gel (Invitrogen), operated with MES SDS running buffer (Invitrogen). For analysis of samples from limited proteolysis, aliquots of the stopped protease digests were mixed with 10 μL of NuPAGE LDS sample buffer (4 \times) (Invitrogen) buffer, and 20 μL of these samples was loaded onto a 4–12% NuPAGE Bis-Tris gel (Invitrogen) run with MES SDS running buffer (Invitrogen). All gels were stained with using Coomassie brilliant blue dye.

Diffusion into an Agarose Gel. A 1.5% agarose gel was cast in phosphate buffered saline (PBS) and immersed within PBS. Oligomer and fibril samples were diluted with NativePAGE

sample buffer (4 \times). Final amounts of 30 μg oligomers and fibrils were loaded and left for 2 h at room temperature. Then the gel was then stained using Coomassie brilliant blue.

Preparation of Fluorescently Labeled $\text{A}\beta$ and Oligomers. The Glu3Cys variant of $\text{A}\beta(1-40)$ was obtained from JPT Peptide (Berlin) through a custom chemical synthesis. Covalent thiol modification was accomplished by coupling to the Alexa Fluor 488-, Alexa Fluor 647-maleimide (Invitrogen), or fluorescein-5-maleimide (Sigma-Aldrich). To that end, we dissolved 1.5 mg of Glu3Cys- $\text{A}\beta(1-40)$ in 100 mM sodium phosphate buffer, pH 7.0, and added 0.5 mg of the dye-maleimide in 65 μL of *N,N*-dimethylformamide. This mixture was kept for 2 h at room temperature under permanent stirring. Unbound dye was removed from the fluorescently labeled peptide by reversed-phase chromatography, and the product purity and identity were verified by high-performance liquid chromatography and electrospray ionization mass spectrometry.

We then prepared three different types of fluorescently labeled oligomers: (i) oligomers containing only AF488- $\text{A}\beta$, (ii) oligomers containing only AF647- $\text{A}\beta$, and (iii) oligomers containing a 1:1 mixture of AF488- $\text{A}\beta$ and AF647- $\text{A}\beta$. In all cases, AF488- $\text{A}\beta$ and AF647- $\text{A}\beta$ were separately dissolved in 100% HFIP at 4 μM concentration. Afterward, the dissolved labeled peptides were mixed with unlabeled $\text{A}\beta(1-40)$ peptide that was dissolved at 396 μM concentration in 100% HFIP. The resulting samples contained final concentrations of 198 μM unlabeled $\text{A}\beta$ and 2 μM AF488- $\text{A}\beta$ (oligomer type (i)) or 2 μM AF647- $\text{A}\beta$ (oligomer type (ii)). To obtain double-labeled oligomers (type (iii)), we first mixed the two labeled peptides in HFIP at 1:1 molar ratio prior to further dilution with unlabeled $\text{A}\beta(1-40)$. Peptide concentrations were confirmed by measurement of dye absorption at 494 nm (AF488, $\epsilon_M = 71\,000\text{ cm}^{-1}\text{ M}^{-1}$) or 650 nm (AF647, $\epsilon_M = 239\,000\text{ cm}^{-1}\text{ M}^{-1}$). The subsequent steps of oligomer preparation were identical to the standard protocol.²⁹ The resulting samples contained 0.2 μM AF488- $\text{A}\beta$ (type (i)) or AF647- $\text{A}\beta$ (type (iii)) together with 19.8 μM unlabeled $\text{A}\beta$ or (type (iii)) 0.1 μM AF488- $\text{A}\beta$ and 0.1 μM AF647- $\text{A}\beta$ with 19.8 μM unlabeled $\text{A}\beta$ in 10% HFIP.

Fluorescence Spectroscopy. All fluorescence measurements were carried out at $20\text{ }^\circ\text{C}$ on a Fluoromax2 spectrometer (Jobin Yvon Spex) using a microcell cuvette filled with a total volume of 160 μL . Emission spectra were recorded at an excitation wavelength of 470 nm (3 nm bandwidth) from 480 to 800 nm (3 nm bandwidth). Excitation spectra were recorded between 350 and 670 nm (2 nm bandwidth) at an emission wavelength of 680 nm (3 nm bandwidth). All spectra were corrected for buffer fluorescence and device-specific effects. Samples for donor-only and acceptor-only reference spectra were obtained by mixing type (i) or type (ii) oligomer preparations with 20 μM unlabeled oligomers 1:1 (v/v) to yield a total labeled $\text{A}\beta$ concentration of 100 nM in each sample, respectively. Spectra of the positive control were recorded from sample type (iii) without prior dilution.

Kinetics to test for subunit exchange was started by combining 2 mL of AF488- $\text{A}\beta$ oligomer stock (type (i)), containing 0.2 μM labeled and 19.8 μM unlabeled peptide, with 2 mL of AF647- $\text{A}\beta$ oligomer stock (type (ii)), containing 0.2 μM labeled and 19.8 μM unlabeled peptide. The final stoichiometric composition of the resulting sample was identical to the oligomer preparation type (iii), which was used as a positive control. However, subunit exchange had to occur in this sample to allow for FRET. The time-dependent buildup of a FRET signal was determined by withdrawing aliquots at different time points and through excitation spectra measurements. Excitation spectra obtained were normalized to the acceptor excitation band at 653 nm, and the time course of subunit exchange was followed at 494 nm and normalized to the intensity of the control sample (100%). Time course of FRET development was fitted using a double-exponential rate law according to

$$y = y_0 + A_1 e^{-k_1 t} + A_2 e^{-k_2 t}$$

Synthesis and Functionalization of FeO. Superparamagnetic iron oxide was synthesized by coprecipitation of Fe^{2+} and Fe^{3+} ions,⁶⁴ separated by an external magnet and washed twice with water and methanol to remove residual reactants. Subsequently,

the superparamagnetic iron oxide was coated with polymethacrylate functionalized by molecular imprinting for specific recognition of the template molecule fluorescein.^{65,66} The polymer-coated FeO was washed to remove all chemical reactants including fluorescein. Before being used, the particle suspensions were dispersed by ultrasound, and the absence of agglomeration was assured by analysis in a Zetasizer Nano ZS90 (Malvern Instruments, UK). FeO was coupled to fluorescein-labeled A β oligomers in a 1:100 ratio (nanoparticle/A β peptides). Particles with attached A β (FeO-A β) were collected by a magnet and washed to remove unbound A β oligomers. FeO-A β particles were resuspended in complete medium and added to cells as indicated.

Physicochemical Characterization of the Iron Oxide Nanoparticles. The average particle size, polydispersity index, conductivity, and zeta-potential were determined by dynamic light scattering using a Zetasizer Nano ZS90. The particle diameter of the polymer-coated iron oxide nanoparticles is 39 nm; the polydispersity index is 0.246; the zeta-potential is -35 mV (measured in 10 mM phosphate buffer, pH 7.4), and conductivity is 1.16 mS/cm.

Cell Culture. Human PBMCs were isolated from fresh blood samples or blood buffy coats by density gradient centrifugation. Macrophages were differentiated from monocytes with 15 ng/mL macrophage colony stimulating factor (GenScript, Piscataway, NJ) and 10% fetal calf serum in RPMI 1640 for 7 days.⁶⁷

Cellular Uptake of A β Oligomers and FeO-A β Particles. Primary human macrophages and PBMCs were incubated with fluorescein- or AF488-labeled A β oligomers (equivalent to 1.15 μ M A β peptides) or 30 μ g Fe/mL FeO-A β particles for up to 6 h. Unbound oligomers were removed by treatment with trypsin/EDTA for 5 min at 37 °C. Particle and A β oligomer internalization was analyzed by flow cytometry (BD Biosciences, Heidelberg, Germany) and confocal microscopy (LSM 710, Zeiss). Flow cytometry data were analyzed using FlowJo 7.6.5 (Treestar, Ashland, OR), and 3D projection from single cells was created using ZEN Software (Zeiss).

Measurement of Intracellular Iron. Intracellular iron contents were detected using bathophenanthroline disulfonic acid as previously described.^{68–70} FeCl₂ was used to generate a standard curve.

Conflict of Interest: The authors declare no competing financial interest.

Acknowledgment: The authors thank J. Ollesch for technical advice on FTIR. The Leibniz Institute for Age Research is financially supported by the State of Thuringia and the Federal Government of Germany. M.F. is supported by DFG (SFB 610), the country Sachsen-Anhalt (Exzellenznetzwerk Biowissenschaften), and BMBF (BioFuture).

Supporting Information Available: Supplementary Table 1. Decomposition of the amide I band of A β (1–40) oligomers and fibrils. Figure S1. Near-spherical morphology of the investigated oligomers. Figure S2. Component analysis of the amide I region of A β oligomers and amyloid fibrils. Figure S3. Fluorescence spectra of single and double labeled oligomers. Figure S4. Temporal development of the FRET signal of single labeled oligomers after mixing. This material is available free of charge via the Internet at <http://pubs.acs.org>.

REFERENCES AND NOTES

- Chiti, F.; Dobson, C. M. Protein Misfolding, Functional Amyloid, and Human Disease. *Annu. Rev. Biochem.* **2006**, *75*, 333–366.
- Toyama, B. H.; Weissman, J. S. Amyloid Structure: Conformational Diversity and Consequences. *Annu. Rev. Biochem.* **2011**, *80*, 557–585.
- Kapurniotu, A. Targeting alpha-Synuclein in Parkinson's Disease. *Chem. Biol.* **2004**, *11*, 1476–1478.
- Fändrich, M. Oligomeric Intermediates in Amyloid Formation: Structure Determination and Mechanisms of Toxicity. *J. Mol. Biol.* **2012**, *421*, 427–440.
- Glaabe, C. G. Structural Classification of Toxic Amyloid Oligomers. *J. Biol. Chem.* **2008**, *283*, 29639–29643.
- Kayed, R.; Head, E.; Thompson, J. L.; McIntire, T. M.; Milton, S. C.; Cotman, C. W.; Glabe, C. G. Common Structure of Soluble Amyloid Oligomers Implies Common Mechanism of Pathogenesis. *Science* **2003**, *300*, 486–489.
- Haass, C.; Selkoe, D. J. Soluble Protein Oligomers in Neurodegeneration: Lessons from the Alzheimer's Amyloid beta-Peptide. *Nat. Rev. Mol. Cell Biol.* **2007**, *8*, 101–112.
- Campioni, S.; Mannini, B.; Zampagni, M.; Pensalfini, A.; Parrini, C.; Evangelisti, E.; Relini, A.; Stefani, M.; Dobson, C. M.; Cecchi, C.; et al. A Causative Link between the Structure of Aberrant Protein Oligomers and Their Toxicity. *Nat. Chem. Biol.* **2010**, *6*, 140–147.
- Bolognesi, B.; Kumita, J. R.; Barros, T. P.; Esbjorner, E. K.; Luheshi, L. M.; Crowther, D. C.; Wilson, M. R.; Dobson, C. M.; Favrin, G.; Yerbury, J. J. ANS Binding Reveals Common Features of Cytotoxic Amyloid Species. *ACS Chem. Biol.* **2010**, *5*, 735–740.
- Krishnan, R.; Goodman, J. L.; Mukhopadhyay, S.; Pacheco, C. D.; Lemke, E. A.; Deniz, A. A.; Lindquist, S. Conserved Features of Intermediates in Amyloid Assembly Determine Their Benign or Toxic States. *Proc. Natl. Acad. Sci. U.S.A.* **2012**, *109*, 11172–11177.
- Nelson, R.; Eisenberg, D. Recent Atomic Models of Amyloid Fibril Structure. *Curr. Opin. Struct. Biol.* **2006**, *16*, 260–265.
- Makin, O. S.; Serpell, L. C. Structures for Amyloid Fibrils. *FEBS J.* **2005**, *272*, 5950–5961.
- Glaabe, C. G. Common Mechanisms of Amyloid Oligomer Pathogenesis in Degenerative Disease. *Neurobiol. Aging* **2006**, *27*, 570–575.
- Linse, S.; Cabaleiro-Lago, C.; Xue, W. F.; Lynch, I.; Lindman, S.; Thulin, E.; Radford, S. E.; Dawson, K. A. Nucleation of Protein Fibrillation by Nanoparticles. *Proc. Natl. Acad. Sci. U.S.A.* **2007**, *104*, 8691–8696.
- Knowles, T. P.; Buehler, M. J. Nanomechanics of Functional and Pathological Amyloid Materials. *Nat. Nanotechnol.* **2011**, *6*, 469–479.
- Fowler, D. M.; Koulov, A. V.; Balch, W. E.; Kelly, J. W. Functional Amyloid—From Bacteria to Humans. *Trends Biochem. Sci.* **2007**, *32*, 217–224.
- Greenwald, J.; Riek, R. Biology of Amyloid: Structure, Function, and Regulation. *Structure* **2010**, *18*, 1244–1260.
- Dueholm, M. S.; Petersen, S. V.; Sønderkær, M.; Larsen, P.; Christiansen, G.; Hein, K. L.; Enghild, J. J.; Nielsen, J. L.; Nielsen, K. L.; Nielsen, P. H.; et al. Functional Amyloid in *Pseudomonas*. *Mol. Microbiol.* **2010**, *77*, 1009–1020.
- Scheibel, T.; Parthasarathy, R.; Sawicki, G.; Lin, X. M.; Jaeger, H.; Lindquist, S. L. Conducting Nanowires Built by Controlled Self-Assembly of Amyloid Fibers and Selective Metal Deposition. *Proc. Natl. Acad. Sci. U.S.A.* **2003**, *100*, 4527–4532.
- Cherny, I.; Gazit, E. Amyloids: Not Only Pathological Agents but Also Ordered Nanomaterials. *Angew. Chem., Int. Ed.* **2008**, *47*, 4062–4069.
- Reches, M.; Gazit, E. Casting Metal Nanowires within Discrete Self-Assembled Peptide Nanotubes. *Science* **2003**, *300*, 625–627.
- Banwell, E. F.; Abelardo, E. S.; Adams, D. J.; Birchall, M. A.; Corrigan, A.; Donald, A. M.; Kirkland, M.; Serpell, L. C.; Butler, M. F.; Woolfson, D. N. Rational Design and Application of Responsive alpha-Helical Peptide Hydrogels. *Nat. Mater.* **2009**, *8*, 596–600.
- Toyama, B. H.; Weissman, J. S. Amyloid Structure: Conformational Diversity and Consequences. *Annu. Rev. Biochem.* **2011**, *80*, 557–585.
- Fändrich, M.; Schmidt, M.; Grigorieff, N. Recent Progress in Understanding Alzheimer's β -Amyloid Structures. *Trends Biochem. Sci.* **2011**, *36*, 338–345.
- Schmidt, M.; Sachse, C.; Richter, W.; Xu, C.; Fändrich, M.; Grigorieff, N. Comparison of Alzheimer A β (1–40) and A β (1–42) Amyloid Fibrils Reveals Similar Protofilament Structures. *Proc. Natl. Acad. Sci. U.S.A.* **2009**, *106*, 19813–19818.
- Sachse, C.; Grigorieff, N.; Fändrich, M. Nanoscale Flexibility Parameters of Alzheimer Amyloid Fibrils Determined by

Electron Cryo-Microscopy. *Angew. Chem., Int. Ed.* **2010**, *49*, 1321–1323.

27. Knowles, T. P.; Fitzpatrick, A. W.; Meehan, S.; Mott, H. R.; Vendruscolo, M.; Dobson, C. M.; Welland, M. E. Role of Intermolecular Forces in Defining Material Properties of Protein Nanofibrils. *Science* **2007**, *318*, 1900–1903.

28. Chimon, S.; Shaibat, M. A.; Jones, C. R.; Calero, D. C.; Aizezi, B.; Ishii, Y. Evidence of Fibril-like β -Sheet Structures in a Neurotoxic Amyloid Intermediate of Alzheimer's β -Amyloid. *Nat. Struct. Mol. Biol.* **2007**, *14*, 1157–1164.

29. Ahmed, M.; Davis, J.; Aucoin, D.; Sato, T.; Ahuja, S.; Aimoto, S.; Elliott, J. I.; Van Nostrand, W. E.; Smith, S. O. Structural Conversion of Neurotoxic Amyloid- β (1–42) Oligomers to Fibrils. *Nat. Struct. Mol. Biol.* **2010**, *17*, 561–567.

30. Haupt, C.; Leppert, J.; Rönicke, R.; Meinhardt, J.; Yadav, J. K.; Ramachandran, R.; Ohlenschläger, O.; Reymann, K. G.; Görlich, M.; Fändrich, M. Structural Basis of β -Amyloid-Dependent Synaptic Dysfunctions. *Angew. Chem., Int. Ed.* **2012**, *51*, 1576–1579.

31. Lopez Del Amo, J. M.; Fink, U.; Dasari, M.; Grelle, G.; Wanker, E. E.; Bieschke, J.; Reif, B. Structural Properties of EGCG-Induced, Nontoxic Alzheimer's Disease $\text{A}\beta$ Oligomers. *J. Mol. Biol.* **2012**, *421*, 517–524.

32. Laganowsky, A.; Liu, C.; Sawaya, M. R.; Whitelegge, J. P.; Park, J.; Zhao, M.; Pensalfini, A.; Soriaga, A. B.; Landau, M.; Teng, P. K.; et al. Atomic View of a Toxic Amyloid Small Oligomer. *Science* **2012**, *335*, 1228–1231.

33. Pedersen, J. S.; Andersen, C. B.; Otzen, D. E. Amyloid Structure—One but Not the Same: The Many Levels of Fibrillar Polymorphism. *FEBS J.* **2010**, *277*, 4591–4601.

34. Habicht, G.; Haupt, C.; Friedrich, R. P.; Hortschansky, P.; Sachse, C.; Meinhardt, J.; Wielgmann, K.; Gellermann, G. P.; Brodhun, M.; Götz, J.; et al. Directed Selection of a Conformational Antibody Domain that Prevents Mature Amyloid Fibril Formation by Stabilizing $\text{A}\beta$ Protomeric. *Proc. Natl. Acad. Sci. U.S.A.* **2007**, *104*, 19232–19237.

35. Stroud, J. C.; Liu, C.; Teng, P. K.; Eisenberg, D. Toxic Fibrillar Oligomers of Amyloid- β Have Cross- β Structure. *Proc. Natl. Acad. Sci. U.S.A.* **2012**, *109*, 7717–7722.

36. Hoshino, M.; Katou, H.; Yamaguchi, K.; Goto, Y. Dimethylsulfoxide-Quenched Hydrogen/Deuterium Exchange Method To Study Amyloid Fibril Structure. *Biochim. Biophys. Acta, Biomembr.* **2007**, *1768*, 1886–1899.

37. Vilar, M.; Wang, L.; Riek, R. Structural Studies of Amyloids by Quenched Hydrogen-Deuterium Exchange by NMR. *Methods Mol. Biol.* **2012**, *849*, 185–198.

38. Pan, J.; Han, J.; Borchers, C. H.; Konermann, L. Structure and Dynamics of Small Soluble $\text{A}\beta$ (1–40) Oligomers Studied by Top-Down Hydrogen Exchange Mass Spectrometry. *Biochemistry* **2012**, *51*, 3694–3703.

39. Luhrs, T.; Ritter, C.; Adrian, M.; Riek-Lohr, D.; Bohrmann, B.; Döbeli, H.; Schubert, D.; Riek, R. 3D Structure of Alzheimer's Amyloid- β (1–42) Fibrils. *Proc. Natl. Acad. Sci. U.S.A.* **2005**, *102*, 17342–17347.

40. Meinhardt, J.; Sachse, C.; Hortschansky, P.; Grigorieff, N.; Fändrich, M. $\text{A}\beta$ (1–40) Fibril Polymorphism Implies Diverse Interaction Patterns in Amyloid Fibrils. *J. Mol. Biol.* **2009**, *386*, 869–877.

41. Colletier, J. P.; Laganowsky, A.; Landau, M.; Zhao, M.; Soriaga, A. B.; Goldschmidt, L.; Flot, D.; Cascio, D.; Sawaya, M. R.; Eisenberg, D. Molecular Basis for Amyloid-beta Polymorphism. *Proc. Natl. Acad. Sci. U.S.A.* **2011**, *108*, 16938–16943.

42. Kodali, R.; Williams, A. D.; Chemuru, S.; Wetzel, R. $\text{A}\beta$ (1–40) Forms Five Distinct Amyloid Structures Whose beta-Sheet Contents and Fibril Stabilities are Correlated. *J. Mol. Biol.* **2010**, *401*, 503–517.

43. Scheidt, H. A.; Morgado, I.; Rothmund, S.; Huster, D.; Fändrich, M. Solid-State NMR Spectroscopic Investigation of $\text{A}\beta$ Protomeric: Implication of a β -Sheet Remodeling upon Maturation into Terminal Amyloid Fibrils. *Angew. Chem., Int. Ed.* **2011**, *50*, 2837–2840.

44. Kanwar, R. K.; Chaudhary, R.; Tsuzuki, T.; Kanwar, J. R. Emerging Engineered Magnetic Nanoparticulate Probes for Molecular MRI of Atherosclerosis: How Far Have We Come?. *Nanomedicine* **2012**, *7*, 899–916.

45. Soppimath, K. S.; Aminabhavi, T. M.; Kulkarni, A. R.; Rudzinski, W. E. Biodegradable Polymeric Nanoparticles as Drug Delivery Devices. *J. Controlled Release* **2001**, *70*, 1–20.

46. Maji, S. K.; Schubert, D.; Rivier, J. E.; Rivier, C.; Lee, S.; Riek, R. Amyloid as Depot for the Formulation of Long-Acting Drugs. *PLoS Biol.* **2008**, *6*, e17.

47. Maji, S. K.; Perrin, M. H.; Sawaya, M. R.; Jessberger, S.; Vadodaria, K.; Rissman, R. A.; Singru, P. S.; Nilsson, K. P.; Simon, R.; Schubert, D.; et al. Functional Amyloids as Natural Storage of Peptide Hormones in Pituitary Secretory Granules. *Science* **2009**, *325*, 328–332.

48. Panyam, J.; Labhasetwar, V. Biodegradable Nanoparticles for Drug and Gene Delivery to Cells and Tissue. *Adv. Drug Delivery Rev.* **2003**, *55*, 329–347.

49. Paul, D. R.; Robeson, L. M. Polymer Nanotechnology: Nanocomposites. *Polymer* **2008**, *49*, 3187–3204.

50. Ehrnhoefer, D. E.; Bieschke, J.; Boeddrich, A.; Herbst, M.; Masino, L.; Lurz, R.; Engemann, S.; Pastore, A.; Wanker, E. E. EGCG Redirects Amyloidogenic Polypeptides into Unstructured, Off-Pathway Oligomers. *Nat. Struct. Mol. Biol.* **2008**, *15*, 558–566.

51. Wynn, T. A.; Chawla, A.; Pollard, J. W. Macrophage Biology in Development, Homeostasis and Disease. *Nature* **2013**, *496*, 445–455.

52. Libby, P.; DiCarli, M.; Weissleder, R. The Vascular Biology of Atherosclerosis and Imaging Targets. *J. Nucl. Med.* **2010**, *51*, 33S–37S.

53. Pankhurst, Q. A.; Connolly, J.; Jones, S. K.; Dobson, J. Applications of Magnetic Nanoparticles in Biomedicine. *J. Phys. D: Appl. Phys.* **2003**, *36*, R167.

54. Ittrich, H.; Peldschus, K.; Raabe, N.; Kaul, M.; Adam, G. Superparamagnetic Iron Oxide Nanoparticles in Biomedicine: Applications and Developments in Diagnostics and Therapy. *Rofo* **2013**, *185*, 1149–1166.

55. Kooi, M. E.; Cappendijk, V. C.; Cleutjens, K. B.; Kessels, A. G.; Kitslaar, P. J.; Borgers, M.; Frederik, P. M.; Daemen, M. J.; van Engelshoven, J. M. Accumulation of Ultrasmall Superparamagnetic Particles of Iron Oxide in Human Atherosclerotic Plaques Can Be Detected by *In Vivo* Magnetic Resonance Imaging. *Circulation* **2003**, *107*, 2453–2458.

56. Cohen Tervaert, J. W. Cardiovascular Disease Due to Accelerated Atherosclerosis in Systemic Vasculitides. *Best Pract. Res. Clin. Rheumatol.* **2013**, *27*, 33–44.

57. Christopeit, T.; Hortschansky, P.; Schroeckh, V.; Gührs, K.; Zandomeneghi, G.; Fändrich, M. Mutagenic Analysis of the Nucleation Propensity of Oxidized Alzheimer's beta-Amyloid Peptide. *Protein Sci.* **2005**, *14*, 2125–2131.

58. Garvey, M.; Tepper, K.; Haupt, C.; Knüpfer, U.; Klement, K.; Meinhardt, J.; Horn, U.; Balbach, J.; Fändrich, M. Phosphate and HEPES Buffers Potently Affect the Fibrillation and Oligomerization Mechanism of Alzheimer's $\text{A}\beta$ Peptide. *Biochem. Biophys. Res. Commun.* **2011**, *409*, 385–388.

59. Schanda, P.; Kupce, E.; Brutscher, B. SOFAST-HMQC Experiments for Recording Two-Dimensional Heteronuclear Correlation Spectra of Proteins within a Few Seconds. *J. Biomol. NMR* **2005**, *33*, 199–211.

60. Bartels, C.; Xia, T. H.; Billeter, M.; Güntert, P.; Wüthrich, K. The Program XEASY for Computer-Supported NMR Spectral Analysis of Biological Macromolecules. *J. Biomol. NMR* **1995**, *5*, 1–10.

61. Delaglio, F.; Grzesiek, S.; Vuister, G. W.; Zhu, G.; Pfeifer, J.; Bax, A. NMRPipe: A Multidimensional Spectral Processing System Based on UNIX Pipes. *J. Biomol. NMR* **1995**, *6*, 277–293.

62. Ollesch, J.; Künemann, E.; Glockshuber, R.; Gerwert, K. Prion Protein α -to- β Transition Monitored by Time-Resolved Fourier Transform Infrared Spectroscopy. *Appl. Spectrosc.* **2007**, *61*, 1025–1031.

63. Fändrich, M.; Dobson, C. M. The Behaviour of Polyamino Acids Reveals an Inverse Side Chain Effect in Amyloid Structure Formation. *EMBO J.* **2002**, *21*, 5682–5690.

64. Dresco, P. A.; Zaitsev, V. S.; Gambino, R. J.; Chu, B. Preparation and Properties of Magnetite and Polymer Magnetite Nanoparticles. *Langmuir* **1999**, *15*, 1945–1951.

65. Mosbach, K.; Ramstrom, O. The Emerging Technique of Molecular Imprinting and Its Future Impact on Biotechnology. *Nat. Biotechnol.* **1996**, *14*, 163–170.
66. Cai, D.; Ren, L.; Zhao, H.; Xu, C.; Zhang, L.; Yu, Y.; Wang, H.; Lan, Y.; Roberts, M. F.; Chuang, J. H.; *et al.* A Molecular-Imprint Nanosensor for Ultrasensitive Detection of Proteins. *Nat. Nanotechnol.* **2010**, *5*, 597–601.
67. Cuaz-Perolin, C.; Billiet, L.; Baugé, E.; Copin, C.; Scott-Algara, D.; Genze, F.; Büchele, B.; Syrovets, T.; Simmet, T.; Rouis, M. Antiinflammatory and Antiatherogenic Effects of the NF- κ B Inhibitor Acetyl-11-keto- β -boswellic Acid in LPS-Challenged ApoE^{−/−} Mice. *Arterioscler., Thromb., Vasc. Biol.* **2008**, *28*, 272–277.
68. Lunov, O.; Syrovets, T.; Büchele, B.; Jiang, X.; Röcker, C.; Tron, K.; Nienhaus, G. U.; Walther, P.; Mailänder, V.; Landfester, K.; *et al.* The Effect of Carboxydextrans-Coated Superparamagnetic Iron Oxide Nanoparticles on c-Jun N-Terminal Kinase-Mediated Apoptosis in Human Macrophages. *Biomaterials* **2010**, *31*, 5063–5071.
69. Lunov, O.; Syrovets, T.; Röcker, C.; Tron, K.; Nienhaus, G. U.; Rasche, V.; Mailänder, V.; Landfester, K.; Simmet, T. Lysosomal Degradation of the Carboxydextrans Shell of Coated Superparamagnetic Iron Oxide Nanoparticles and the Fate of Professional Phagocytes. *Biomaterials* **2010**, *31*, 9015–9022.
70. Lunov, O.; Zablotskii, V.; Syrovets, T.; Röcker, C.; Tron, K.; Nienhaus, G. U.; Simmet, T. Modeling Receptor-Mediated Endocytosis of Polymer-Functionalized Iron Oxide Nanoparticles by Human Macrophages. *Biomaterials* **2011**, *32*, 547–555.
71. Scheidt, H. A.; Morgado, I.; Rothemund, S.; Huster, D. Dynamics of Amyloid β Fibrils Revealed by Solid-State NMR. *J. Biol. Chem.* **2012**, *287*, 2017–2021.